

A fractional order derivative based active contour model for inhomogeneous image segmentation



Bo Chen ^{a,b,*}, Shan Huang ^a, Zhengrong Liang ^c, Wensheng Chen ^{a,b}, Binbin Pan ^{a,b}

^a Shenzhen Key Laboratory of Advanced Machine Learning and Applications, College of Mathematics and Statistics, Shenzhen University, Shenzhen 518060, China

^b Shenzhen Key Laboratory of Media Security, Shenzhen University, Shenzhen 518060, China

^c Department of Radiology, State University of New York, Stony Brook, NY, 11790, USA

ARTICLE INFO

Article history:

Received 28 November 2017

Revised 9 August 2018

Accepted 14 August 2018

Available online 23 August 2018

Keywords:

Image segmentation

Inhomogeneous image

Active contour model

Fractional order differentiation

ABSTRACT

Segmenting intensity inhomogeneous images is a challenging task for both local and global methods. Some hybrid methods have great advantages over the traditional methods in inhomogeneous image segmentation. In this paper, a new hybrid method is presented, which incorporates image gradient, local environment and global information into a framework, called adaptive-weighting active contour model. The energy or level set functions in the framework mainly include two parts: a global term and local term. The global term aims to enhance the image contrast, and it can also accelerate the convergence rate when minimizing the energy function. The local term integrates fractional order differentiation, fractional order gradient magnitude, and difference image information into the well-known local Chan–Vese model, which has been shown to be effective and efficient in modeling the local information. The local term can also enhance low frequency information and improve the inhomogeneous image segmentation. An adaptive weighting strategy is proposed to balance the actions of the global and local terms automatically. When minimizing the level set functions, regularization can be imposed by applying Gaussian filtering to ensure smoothness in the evolution process. In addition, a corresponding stopping criterion is proposed to ensure the evolving curve automatically stops on true boundaries of objects. Dice similarity coefficient is employed as the comparative quantitative measures for the segmented results. Experiments on synthetic images as well as real images are performed to demonstrate the segmentation accuracy and computational efficiency of the presented hybrid method.

© 2018 Elsevier Inc. All rights reserved.

1. Introduction

Image segmentation method based on partial differential equation (PDE) shows strong vitality in the fields of image processing and computer vision. Some of the segmentation methods can be seen as linear systems [1], others are nonlinear systems [2,3]. Geometric active contour models (ACMs) [4–10], is a major breakthrough in the application of the PDE methods in image processing, have been widely applied in the fields of image segmentation, denoising and object tracing. It is

* Corresponding author at: College of Mathematics and Statistics, Shenzhen University, Shenzhen 518060, China.

E-mail address: chenbo@szu.edu.cn (B. Chen).

known that ACMs, based on curve evolution and level set theories, can deal with topological change automatically in image segmentation.

In general, ACMs can be categorized into two classes: edge-based models [4,5,7] and region-based models [6,8]. Edge-based models use image gradient information to identify object boundaries and stop the contour evolution. One of them is the famous geodesic active contour model [4], which is derived from the snake model [11] and defines a gradient-based edge detector function. Because of the local limitation, edge-based models are sensitive to image noise and depend on location of initial curve. On the other hand, region-based models employ region information to control the curve evolution and do not depend on the gradient information. Compared to the edge-based models, region-based models have several advantages. For example, region-based models are not so sensitive to noise and can segment images with weak edges. One of the most popular region-based models is Chan–Vese (CV) model [6], which is the curve evolution implementation of a piecewise constant case of the Mumford–Shah (MS) model [12] and has been applied to binary phase image segmentation successfully [6]. However, the CV model often leads to inferior results in inhomogeneous image segmentation because it assumes that each region is statistically homogeneous and the intensities within the area of foreground and background always maintain constant, respectively. To overcome this defect, many methods have been proposed to improve the performance of segmenting intensity inhomogeneity images. For example, Vese and Chan [13] and Tsai et al. [14] proposed two similar region-based active contour models by minimizing the MS functional [12], which replaced the piece-wise constant intensity by piece-wise smooth intensity, called piece-wise smooth (PS) models hereafter. Although these PS models have exhibited certain capability of handling the intensity inhomogeneity, they are computationally expensive and the gain in segmentation accuracy is limited. The advantages and limitations of these efforts to relieve the piece-wise constant assumption are also seen from the following examples. Li et al. [15] proposed a local binary fitting (LBF) model by incorporating a kernel function to define local binary fitting energy in a variational formulation. Liu and Peng [16] proposed a local region-based Chan–Vese model by considering the image local characteristics. Wang et al. [8] proposed an alternative local Chan–Vese model (LCV) by utilizing the difference image information. It is clearly seen that an alternative approach is desired.

Recently, fractional order differentiation was explored in differential equation systems [17–19] and applied in the field of image processing [20–22]. It shows that the model based on fractional order differentiation has an advantage over the above region-based models [20,22]. Mathieu et al. [23] proposed a new model which integrated local edge detector with fractional differentiation. Nakib et al. [24] gave a new geometric interpretation of two dimensional (2D) fractional differentiation and applied it to threshold segmentation. Ren [25] proposed an adaptive active contour model with a fractional order fitting energy. From the view of theory analysis, fractional order differentiation can be defined or expressed in different domains: one is spatial domain expression, such as Riemann–Liouville fractional order differentiation and Grünwald–Letnikov fractional order differentiation; and the other is frequency-domain expression. Each of the expressions has its advantages. In this paper, we employ frequency-domain fractional order differentiation expression and apply it to segment inhomogeneity images.

In addition to the recent interest in fractional order differentiation, another technique, called re-initialization, which was used for re-initializing a level set function to a signed distance function during evolution, has also attracted great interests as a numerical method to maintain stable curve evolution and ensure desirable results as the models or cost functions becomes more sophisticated. Theoretically, re-initialization is not necessary if a cost function is globally concave and its maximum point can be reached in finite iteration steps. However, the condition frequently cannot be satisfied in practice. To avoid re-initialization, Li et al. [26] proposed a variational level set formulation with a penalty term that automatically forces the level set function to be close to a signed distance function. While this strategy has been successfully applied in many variational active contour models, the computational efficiency is relatively low. To improve the efficiency, Zhang et al. [27] proposed a novel region-based active contour model, named selective binary and Gaussian filtering regularized level set segmentation method, which uses a Gaussian kernel to regularize the level-set function after each iteration step. It not only regularizes the level set, but also removes the need of computationally expensive re-initialization. Because of those advantages, this study will consider this kernel approach for the frequency-domain fractional order differentiation expression.

Since the fractional order differentiation has the properties of preserving and highly likely enhancing low frequency information, where the low frequency information reflects very important characteristics of pieces-wise smooth inhomogeneous images, thus this paper intends to explore a new active contour model based on Fourier domain fractional order differentiation for segmenting inhomogeneous images. A novel adaptive weighting strategy is also included in our new model to adjust the action of the involved global and local terms automatically. We further adopt the Gaussian filtering re-initialization strategy to regularize our level set function to ensure a smooth level set function evolution toward a desired result. Furthermore, a new stopping criterion, based on the change of the area inside the evolving curve, is proposed, which can automatically stop on true boundaries of the objects in limited iterations. Experimental results from synthetic and real images in this study show that the proposed inhomogeneity image segmentation method is more efficient and effective than traditional methods.

The rest of the paper is organized as follows. Section 2 briefly reviews some related classical models and their backgrounds. Section 3 describes our model and its variational formulation. In Section 4, we validate our method by various experiments on synthetic and real images. Finally, some conclusive remarks are included in Section 5.

2. The related models and backgrounds

2.1. CV model

CV model [6] is a classical active contour segmentation model derived from MS model [12]. The basic idea of the CV model is to utilize regional mean gray values to decide the contour and divide the image into the targets and background. Let $\Omega \subset \mathbb{R}^2$ be the image domain, and $I(x, y): \Omega \rightarrow \mathbb{R}$ is a given image function, where x, y represent horizontal and vertical coordinates of pixels, separately, and $I(x, y)$ denotes the intensity at a point (x, y) . The basic CV model is formulated by minimizing the following energy functional:

$$E^{CV}(C, c_1, c_2) = \lambda_1 \int_{inside(C)} |I(x, y) - c_1|^2 dx dy + \lambda_2 \int_{outside(C)} |I(x, y) - c_2|^2 dx dy \quad (1)$$

where $\lambda_1, \lambda_2 > 0$ are fixable parameters, $inside(C)$, $outside(C)$ represent the region inside and outside of the contour C , respectively, and c_1, c_2 are two constants, which are the average intensities inside and outside the contour C , separately. With the level set function ϕ , we assume:

$$\begin{cases} C = \{(x, y) \in \Omega : \phi(x, y) = 0\} \\ inside(C) = \{(x, y) \in \Omega : \phi(x, y) > 0\} \\ outside(C) = \{(x, y) \in \Omega : \phi(x, y) < 0\} \end{cases} \quad (2)$$

By minimizing Eq. (1), we can obtain c_1 and c_2 :

$$\begin{cases} c_1 = \frac{\int_{\Omega} I(x, y) H(\phi(x, y)) dx dy}{\int_{\Omega} H(\phi(x, y)) dx dy} \\ c_2 = \frac{\int_{\Omega} I(x, y) (1 - H(\phi(x, y))) dx dy}{\int_{\Omega} (1 - H(\phi(x, y))) dx dy} \end{cases} \quad (3)$$

where $H(\phi)$ is the Heaviside function. By introducing a length term $\int_{\Omega} |\nabla H(\phi(x, y))| dx dy$ (where ∇ represents the gradient operator) and an area term $\int_{\Omega} H(\phi(x, y)) dx dy$, which are used to regularize the contour, into Eq. (1), then minimizing Eq. (1) and the added terms together, we can obtain the following variational formulation:

$$\frac{\partial \phi}{\partial t} = \delta(\phi) \left[\mu \operatorname{div} \left(\frac{\nabla \phi}{|\nabla \phi|} \right) - v - \lambda_1 (I - c_1)^2 + \lambda_2 (I - c_2)^2 \right] \quad (4)$$

where parameters $\mu \geq 0, v \geq 0$, μ controls the smoothness of zero level set, and v increases the propagation speed. Notation $\delta(\phi)$ indicates the Dirac function and it is defined as the derivative of the Heaviside function $H(\phi)$:

$$H(z) = \begin{cases} 1, & z \geq 0 \\ 0, & z < 0, \end{cases} \quad \delta(z) = \frac{d}{dz} H(z) = \begin{cases} 0, & z \neq 0 \\ +\infty, & z = 0 \end{cases}$$

In order to compute the partial differential equation in Eq. (4), discontinuous functions $H(\phi)$ and $\delta(\phi)$ need to be approximated by regularized version $H_{\varepsilon}(\phi), \delta_{\varepsilon}(\phi)$. In general, the regularized Heaviside function and Dirac function are selected as follows:

$$\begin{cases} H_{\varepsilon}(z) = \frac{1}{2} \left(1 + \frac{2}{\pi} \arctan \left(\frac{z}{\varepsilon} \right) \right) \\ \delta_{\varepsilon}(z) = \frac{1}{\pi} \cdot \frac{\varepsilon}{\varepsilon^2 + z^2}, z \in \mathbb{R} \end{cases} \quad (5)$$

where \mathbb{R} represents the set of real number and ε is a small value in the denominator to avoid the singularities. ε is also a predefined parameter for control the speed of the function $H_{\varepsilon}(z)$ rising from 0 to 1. As shown in Fig. 1, when $\varepsilon \rightarrow 0$, regularized functions $H_{\varepsilon}(z), \delta_{\varepsilon}(z)$ converges to $H(z)$ and $\delta(z)$, respectively. On the other hand, for a fixed ε , we set it to 1 in our experiment, the regularized Heaviside function $H_{\varepsilon}(z)$ converges to 1 when $z \rightarrow +\infty$, when $z \rightarrow -\infty$, function $H_{\varepsilon}(z)$ converges to 0.

The parameters also can be set as $\lambda_1 = \lambda_2, v = 0$. μ is a scaling parameter, if it is small enough, small objects are likely to be extracted, if it is large enough, big objects are likely to be detected [6].

CV model has good performance in image segmentation. For example, it performed well for detection of objects whose boundaries are not necessarily defined by gradient or with weak boundaries. However, it generally fails to segment images with intensity inhomogeneity.

2.2. LCV model

Wang et al. [8] proposed LCV model, whose energy functional consists of three parts: global term E^G , local term E^L , and regularization term E^R . The energy functional is defined as follows:

$$E^{LCV} = \lambda_3 E^G + \lambda_4 E^L + E^R \quad (6)$$

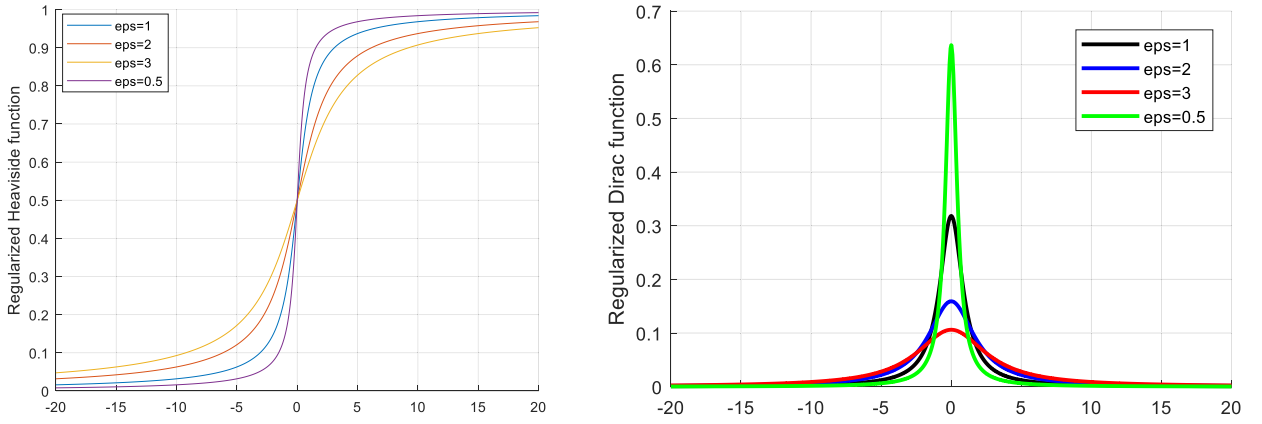


Fig. 1. The regulated Heaviside function (left) and Dirac delta function (right) with different ε .

where λ_3 and λ_4 are fixable parameters, E^G is the same as the energy fitting term of CV model of Eq. (1). For the local term, E^L is defined as follows:

$$\begin{aligned} E^L(C, d_1, d_2) = & \int_{\text{inside}(C)} |g_k * I(x, y) - I(x, y) - d_1|^2 dx dy \\ & + \int_{\text{outside}(C)} |g_k * I(x, y) - I(x, y) - d_2|^2 dx dy \end{aligned} \quad (7)$$

where g_k is an averaging convolution operator with $k \times k$ size window, d_1 and d_2 are the intensity average of the difference image ($g_k * I(x, y) - I(x, y)$) inside and outside C , respectively, and it is defined as follows:

$$\begin{cases} d_1 = \frac{\int_{\Omega} (g_k * I(x, y) - I(x, y)) H_{\varepsilon}(\phi(x, y)) dx dy}{\int_{\Omega} H_{\varepsilon}(\phi(x, y)) dx dy} \\ d_2 = \frac{\int_{\Omega} (g_k * I(x, y) - I(x, y))(1 - H_{\varepsilon}(\phi(x, y))) dx dy}{\int_{\Omega} (1 - H_{\varepsilon}(\phi(x, y))) dx dy} \end{cases} \quad (8)$$

For the regularization term, E^R is defined by:

$$E^R = \gamma \int_{\Omega} |\nabla H_{\varepsilon}(\phi(x, y))| dx dy + \int_{\Omega} \frac{1}{2} (|\nabla \phi(x, y)| - 1)^2 dx dy \quad (9)$$

By introducing the local term E^L , the regularization term E^R and the global term E^G of Eq. (1) into Eq. (6), and further minimizing them together, we can obtain the following variational formulation:

$$\begin{aligned} \frac{\partial \phi}{\partial t} = & \delta_{\varepsilon}(\phi) [-\lambda_3(I(x, y) - c_1)^2 + \lambda_3(I(x, y) - c_2)^2] + \delta_{\varepsilon}(\phi) [-\lambda_4(g_k * I(x, y) \\ & - I(x, y) - d_1)^2 + \lambda_4(g_k * I(x, y) - I(x, y) - d_2)^2] \\ & + \gamma \delta_{\varepsilon}(\phi) \operatorname{div} \left(\frac{\nabla \phi}{|\nabla \phi|} \right) + \Delta \phi - \operatorname{div} \left(\frac{\nabla \phi}{|\nabla \phi|} \right) \end{aligned} \quad (10)$$

where Δ is the Laplace operator and div means the divergence of vector.

2.3. The Fourier domain fractional order differentiation

For a given function of a single variable $f(t)$, the Fourier transform is defined as follows:

$$\hat{f}(\omega) = \int_{\mathbb{R}} f(t) \exp(-j\omega t) dt \quad (11)$$

where \mathbb{R} denotes the set of real number, j is the imaginary unit, i.e., $j = \sqrt{-1}$ and ω is the variable in frequency domain.

According to the differentiation property of Fourier transform, the equivalent formulation of the n th derivative in the Fourier domain is:

$$D^n f = f^n(t) \leftrightarrow \mathcal{F}(f^n(t)) = (j\omega)^n \hat{f}(\omega) \quad (12)$$

where n is a nonnegative integer, “ \leftrightarrow ” represents the Fourier transform pair. It can be shown straightforwardly that the Fourier domain expression of the α th-order differentiation, $D^\alpha f(t)$, is $(j\omega)^\alpha \hat{f}(\omega)$, where the α can be any positive real

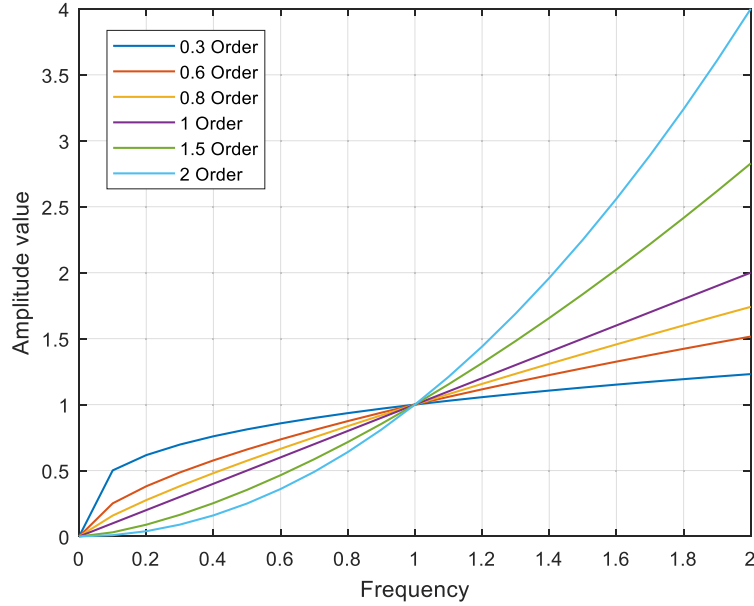


Fig. 2. Amplitude–frequency curve of fractional order differential operator.

number. Thus, the fractional order differentiation expression of the function $f(t)$ in frequency domain is defined as:

$$D^\alpha f(t) = \mathcal{F}^{-1}((j\omega)^\alpha \hat{f}(\omega)), \quad \alpha \in \mathbb{R}^+ \quad (13)$$

where \mathbb{R}^+ is the set of positive real number, and \mathcal{F}^{-1} is the inverse Fourier transform operator.

Refer to Eq. (11), for two-dimensional function $h(p, q)$, its Fourier transform is defined as follows:

$$\hat{h}(\omega_1, \omega_2) = \int \int_{\mathbb{R} \times \mathbb{R}} h(p, q) \exp(-j(\omega_1 p + \omega_2 q)) dp dq \quad (14)$$

Thus, the fractional order partial differentiation of $h(p, q)$ can be defined as follows:

$$\begin{cases} D_p^\alpha h(p, q) = \mathcal{F}^{-1}((j\omega_1)^\alpha \hat{h}(\omega_1, \omega_2)) \\ D_q^\alpha h(p, q) = \mathcal{F}^{-1}((j\omega_2)^\alpha \hat{h}(\omega_1, \omega_2)) \end{cases} \quad (15)$$

For an $m \times m$ image $g(x, y)$, its discrete Fourier transform (DFT) can be calculated as

$$\hat{g}(\omega_1, \omega_2) = \frac{1}{m} \sum_{x=0}^{m-1} \sum_{y=0}^{m-1} g(x, y) \exp(-j2\pi(\omega_1 x + \omega_2 y)/m)$$

According to the translation property of the two-dimension DFT, the difference schemes of the first order derivative in the Fourier domain can be defined as

$$\begin{cases} D_x^\alpha g(x, y) = \mathcal{F}^{-1}((1 - \exp(-j2\pi\omega_1/m))^\alpha \hat{g}(\omega_1, \omega_2)) \\ D_y^\alpha g(x, y) = \mathcal{F}^{-1}((1 - \exp(-j2\pi\omega_2/m))^\alpha \hat{g}(\omega_1, \omega_2)) \end{cases} \quad (16)$$

In practice computations, we adopt centered difference scheme as follow

$$\begin{cases} D_x^\alpha g(x, y) = \mathcal{F}^{-1}((1 - \exp(-j2\pi\omega_1/m))^\alpha \exp(j\pi\alpha w_1/m) \hat{g}(\omega_1, \omega_2)) \\ D_y^\alpha g(x, y) = \mathcal{F}^{-1}((1 - \exp(-j2\pi\omega_2/m))^\alpha \exp(j\pi\alpha w_2/m) \hat{g}(\omega_1, \omega_2)) \end{cases} \quad (17)$$

As we all know, the intensity inhomogeneity is varying slowly in the image domain, and its spectrum in frequency domain will be concentrated in the low frequency area. In Eq. (13), let $(j\omega)^\alpha \hat{f}(\omega) = \hat{d}^\alpha(\omega) \cdot \hat{f}(\omega)$, where $\hat{d}^\alpha(\omega) = (j\omega)^\alpha$ and its complex exponent is as follows

$$\begin{cases} \hat{d}^\alpha(\omega) = (j\omega)^\alpha = \hat{a}^\alpha(\omega) e^{j\hat{\theta}^\alpha(\omega)} \\ \hat{a}^\alpha(\omega) = |\omega|^\alpha, \quad \hat{\theta}^\alpha(\omega) = \frac{\alpha\pi}{2} \operatorname{sgn}(\omega) \end{cases}, \quad \alpha \in \mathbb{R}^+ \quad (18)$$

where $\operatorname{sgn}(\cdot)$ is a sign function, ω denotes frequency, $0 < \omega < 1$ represents low-frequency parts and reflects the intensity inhomogeneity in the image domain. $\omega > 1$ represents high-frequency parts and reflects edges or sharp places of the gray scale change in the image. Fig. 2 shows the amplitude–frequency characteristic of fractional order differentiation. When $0 <$

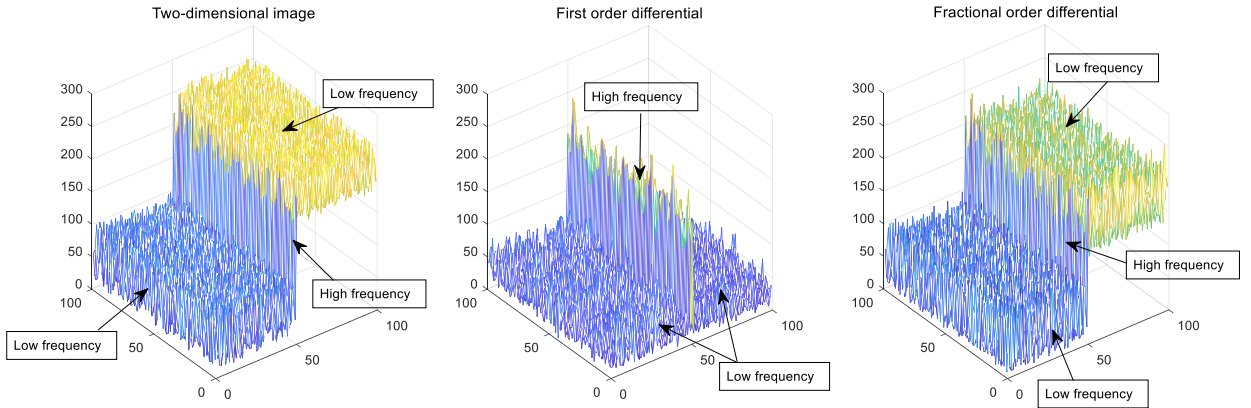


Fig. 3. Contrast of processing result between integer order derivative and fractional order differential.

$\alpha < 1$, fractional order differentiation operator enhances the amplitude of signal, and the magnitude of the ascent is slightly greater than the first and second derivative in the low-frequency part. For high-frequency, fractional order differentiation operator also enhances the amplitude of signal to some extent, but the level of enhancement is significantly less than first and second derivative. It indicates that fractional order differentiation can preserve low frequency in a non-linear manner and enhance the high frequency information. Fig. 3 shows the contrast of processing result between first order differential and fractional order differential in a two-dimensional image.

In the Fourier or frequency domain, the fractional order differentiation can be seen as the generalization of the integer order differentiation [28], but the fractional order differentiation can effectively preserve and highly likely enhance the low frequency information while the integer order differentiation usually shows unsatisfactory performance in these cases [20]. We will present our strategy for the application to segmentation of inhomogeneous images in the next section.

3. The description of the proposed model and its implementation

3.1. The proposed model

Inspired by the most recent segmentation models, the energy functional in our proposed model also consists of three parts: the global term E^G , the local term E^L , and the length (or regularization) term of curve E^R . We adopt the energy fitting of CV model (see Eq. (1)) and length term as our global term E^G and term E^R in our energy functional because of their good performance in various applications. Now we focus on the local term E^L using the Fourier domain fractional order differentiation because of its unique advantages as described above. The details are given below.

Firstly, for a given image $I(X)$ as defined before, where X is a two-dimensional vector, i.e., $X = (x, y)$. The fractional gradient magnitude is introduced with the following definition:

$$\text{mag}(\nabla^\alpha I(X)) = [(D_x^\alpha)^2 + (D_y^\alpha)^2]^{\frac{1}{2}} \quad (19)$$

where D_x^α and D_y^α are defined in Eq. (15), ∇ is the gradient operator, as defined above, ∇^α is the fractional gradient operator. Secondly, a new difference image $u(X)$ is constructed:

$$u(X) = I(X) - \text{mag}(\nabla^\alpha I(X)) \quad (20)$$

Finally, the proposed local energy fitting is defined as follows:

$$E^L(C, m_1(X), m_2(X)) = \int_{\text{inside}(C)} |u(X) - m_1(X)|^2 dX + \int_{\text{outside}(C)} |u(X) - m_2(X)|^2 dX \quad (21)$$

where $m_1(X)$ and $m_2(X)$ are defined as following:

$$\begin{cases} m_1(X) = \frac{\int_{\Omega} G_{\sigma_1}(X - Y) u(Y) H_\varepsilon(\phi(Y)) dY}{\int_{\Omega} G_{\sigma_1}(X - Y) H_\varepsilon(\phi(Y)) dY} \\ m_2(X) = \frac{\int_{\Omega} G_{\sigma_1}(X - Y) u(Y) (1 - H_\varepsilon(\phi(Y))) dY}{\int_{\Omega} G_{\sigma_1}(X - Y) (1 - H_\varepsilon(\phi(Y))) dY} \end{cases} \quad (22)$$

where G_{σ_1} represents the Gaussian kernel function with standard variation σ_1 . The G_{σ_1} has the following local property, i.e., the contribution of the intensity $u(Y)$ to $m_1(X)$ and $m_2(X)$ decreases and approaches to zero as the point Y goes away from the center point X . It is obvious the $m_1(X)$ and $m_2(X)$ are different from the constant d_1 and d_2 of the LCV model.

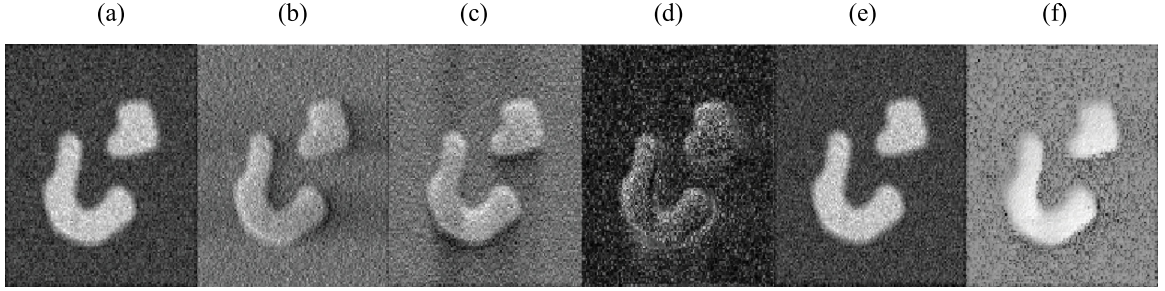


Fig. 4. Images related to fractional order. (a) the original image I ; (b) the fractional order image D_x^α ; (c) the fractional order image D_t^α ; (d) the fractional order gradient magnitude image $\text{mag}(\nabla^\alpha I(X))$; (e) the difference image by subtracting first order differential gradient magnitude from the original image; and (f) the proposed difference image u .

The idea of the proposed local term E^L is comes from three observations. Firstly, intensity inhomogeneity will change slowly in the image domain, thus most of its spectrum in frequency domain will be smaller. At the same time, the fractional order differentiation has shown excellent performance in preserving and enhancing the low frequency information [20]. Thus, fractional order differentiation is employed our model can for improving the performance of segmenting intensity inhomogeneity images. Secondly, the fractional gradient magnitude also inherits the property of the fractional order differentiation. And the gradient magnitude $\text{mag}(\nabla^\alpha I(X))$ (see Fig. 4(d)) is superior to the first order differentiation in terms of enhancement and preservation of low frequency information, and it can improve noise immunity to some extent [25]. This property is important for noisy image processing and has shown good performance when it was applied to many image processing applications [20,25]. Thirdly, when the fractional order gradient magnitude image is subtracted from the original image, the image will become smoother (see Fig. 4(f)) compared with the original image; and the contrast of proposed difference image has been improved compared with the difference image obtained by subtracting first order differential gradient magnitude from the original image (see Fig. 4(e)). Thus, more accurate segmented result can be obtained in an efficient manner. In summary, since the local information, particularly the information from the low-frequency region, is very important for intensity inhomogeneity images segmentation, our proposed local term of enhancing the information from the low-frequency region is a theoretically-innovative and practically-logic model. Some images related to fractional order are shown in Fig. 4, the use of fractional order differentiation, fractional order gradient magnitude and difference image has shown great potential to achieve excellent segmentation performance.

Based on the above analysis of local term E^L , the final energy functional can be described as

$$\begin{aligned}\tilde{E} &= (1-w)E^G + wE^L + \mu E^R \\ &= (1-w)\int_{\Omega}|I(X) - c_1|^2 H_\varepsilon(\phi) dX + (1-w)\int_{\Omega}|I(X) - c_2|^2 (1 - H_\varepsilon(\phi)) dX \\ &\quad + w\int_{\Omega}|u(X) - m_1(X)|^2 H_\varepsilon(\phi) dX + w\int_{\Omega}|u(X) - m_2(X)|^2 (1 - H_\varepsilon(\phi)) dX \\ &\quad + \mu\int_{\Omega}|\nabla H_\varepsilon(\phi)| dX\end{aligned}\quad (23)$$

Utilizing level set method and variational strategy to minimize the proposed energy functional, we can obtain the corresponding gradient descent flow of the energy functional in Eq. (23) (derivation process is given in Appendix):

$$\begin{aligned}\frac{\partial\phi}{\partial t} &= \delta_\varepsilon(\phi)\left\{(1-w)[-(I(X) - c_1)^2 + (I(X) - c_2)^2]\right. \\ &\quad \left.+ w[-(u(X) - m_1(X))^2 + (u(X) - m_2(X))^2] + \mu\text{div}\left(\frac{\nabla\phi}{|\nabla\phi|}\right)\right\}\end{aligned}\quad (24)$$

where w is the weighting parameter between the global term and the local term. As mentioned above, the weighting parameter plays an important role. It will be described below.

For a given initial function, the stationary solution of the gradient descent flow in (24) can be obtained by calculating the associated iterative formulation in Eq. (24). The stationary solution of the gradient descent flow in (24) is also the minimum of the energy functional in (23).

3.2. The adaptive weighting

Wang et al. [29] discussed the problem about the selection of weighting between the global and local terms. When the contour C is evolving close to the object boundaries, the local term should dominate the whole energy; when the curve C is evolving far away from the object boundaries, the global term should dominate the whole energy.

With the above analysis and the inspiration by the previous work in literatures [9,30], we propose an adaptive weighting by the use of the fractional order gradient magnitude information as follows:

$$w(X) = \rho \cdot \text{average}(C_N(X)) \cdot C_N(X) \quad (25)$$

where ρ is a fixed positive parameter and can be generally set to be $\rho=1$, $\text{average}(C_N(X))$ is the arithmetic mean of all $C_N(X)$, and the $C_N(X)$ is a local contrast ratio of a gradient image defined as:

$$C_N(X) = \frac{M_{\max}(u(X)) - M_{\min}(u(X))}{M} \quad (26)$$

where N defines the size of the local window centered at point X , M_{\max} and M_{\min} are the maximum and minimum of intensities within this local window respectively, and M represents the maximum intensity of the image $u(X)$. Thus, C_N varies between 0 and 1, $w(X)$ and $(1-w(X))$ also vary between 0 and 1. When the contour C is evolving far away from the object boundaries, the local intensity varies slowly and the C_N would be small, so the weighting $(1-w(X))$ will be large, and the global term will dominate the whole energy. When the contour C is evolving close to the object boundaries, the local intensity varies greatly and the C_N would be large, so the weighting $w(X)$ will be large, and the local term will dominate the whole energy. Consequently, the adaptive weighting will be automatically adjusted as the evolution is proceeding. We substitute $w(X)$ for the constant w in Eq. (24), and the final proposed variational formulation is as follows:

$$\begin{aligned} \frac{\partial \phi}{\partial t} = & \delta_\varepsilon(\phi) \left\{ (1-w(X))[-(I(X)-c_1)^2 + (I(X)-c_2)^2] \right. \\ & \left. + w(X)[-(u(X)-m_1(X))^2 + (u(X)-m_2(X))^2] + \mu \operatorname{div}\left(\frac{\nabla \phi}{|\nabla \phi|}\right) \right\} \end{aligned} \quad (27)$$

3.3. Numerical algorithm

In applications of image processing, finite difference methods (FDMs) are the common approach for numerical solutions of partial differential equations. In this paper, we adopt a finite difference explicit scheme to discretize Eq. (27). Let Δt be the time step, h be the space step, and $(x_i, y_j) = (ih, jh)$ denotes the grid points, $1 \leq i \leq M, 1 \leq j \leq N$, for an $M \times N$ image. And $\varphi(t, x, y)$ is approximated as $\varphi(n\Delta t, x, y)$, denoted by $\phi_{i,j}^n$ ($n > 0$, denotes the number of iteration). Then, the partial differential equation Eq. (27) can be discretized as following:

$$\begin{aligned} \frac{\phi_{i,j}^{n+1} - \phi_{i,j}^n}{\Delta t} = & \delta_\varepsilon(\phi_{i,j}^n) \{ (1-w_{i,j})[-(l_{i,j}-c_1(\phi^n))^2 + (l_{i,j}-c_2(\phi^n))^2] \\ & + w_{i,j}[-(u_{i,j}-m_{1,i,j}(\phi^n))^2 + (u_{i,j}-m_{2,i,j}(\phi^n))^2] + \mu \cdot \kappa_{i,j}^n \} \end{aligned} \quad (28)$$

where n denotes the number of iteration, $c_1(\phi^n)$, $c_2(\phi^n)$ can be calculated using Eq. (3), and $m_{1,i,j}(\phi^n)$, $m_{2,i,j}(\phi^n)$ can be computed by Eq. (22). $\delta_\varepsilon(\phi_{i,j}^n)$ is calculated by regulated Dirac delta function, refer to Eq. (5).

$$\kappa_{i,j}^n = \operatorname{div}\left(\frac{\nabla \phi_{i,j}^n}{|\nabla \phi_{i,j}^n|}\right) = \frac{\Delta^{xx}\phi_{i,j}^n \cdot (\Delta^y\phi_{i,j}^n)^2 - 2 \cdot \Delta^{xy}\phi_{i,j}^n \cdot \Delta^x\phi_{i,j}^n \cdot \Delta^y\phi_{i,j}^n + \Delta^{yy}\phi_{i,j}^n \cdot (\Delta^x\phi_{i,j}^n)^2}{((\Delta^x\phi_{i,j}^n)^2 + (\Delta^y\phi_{i,j}^n)^2)^{\frac{3}{2}}}$$

All the spatial partial derivatives are approximated by central difference, the discrete form of $\Delta^x\phi_{i,j}^n$, $\Delta^y\phi_{i,j}^n$, $\Delta^{xx}\phi_{i,j}^n$, $\Delta^{yy}\phi_{i,j}^n$ and $\Delta^{xy}\phi_{i,j}^n$ are given by

$$\begin{cases} \Delta^x\phi_{i,j}^n = \frac{\phi_{i+1,j}^n - \phi_{i-1,j}^n}{2h}, & \Delta^y\phi_{i,j}^n = \frac{\phi_{i,j+1}^n - \phi_{i,j-1}^n}{2h}, \\ \Delta^{xx}\phi_{i,j}^n = \frac{\phi_{i+1,j}^n + \phi_{i-1,j}^n - 2\phi_{i,j}^n}{h^2}, & \Delta^{yy}\phi_{i,j}^n = \frac{\phi_{i,j+1}^n + \phi_{i,j-1}^n - 2\phi_{i,j}^n}{h^2}, \\ \Delta^{xy}\phi_{i,j}^n = \frac{\phi_{i+1,j+1}^n - \phi_{i-1,j+1}^n - \phi_{i+1,j-1}^n + \phi_{i-1,j-1}^n}{h^2} \end{cases}$$

3.4. Implementation

When the evolving curve arrives at the position of true boundaries, the curve evolution should stop. Generally, the evolving curve in level set evolution process can automatically stop on true boundaries of objects according to the length change inside the evolving curve [8]. However, the stopping criterion would be more sensitively depending on the area change inside the evolving curve. For this reason, we firstly put forward the following criterion:

$$|\int_{\Omega} H(\phi^{n+1})dX - \int_{\Omega} H(\phi^n)dX| < \eta \quad (29)$$

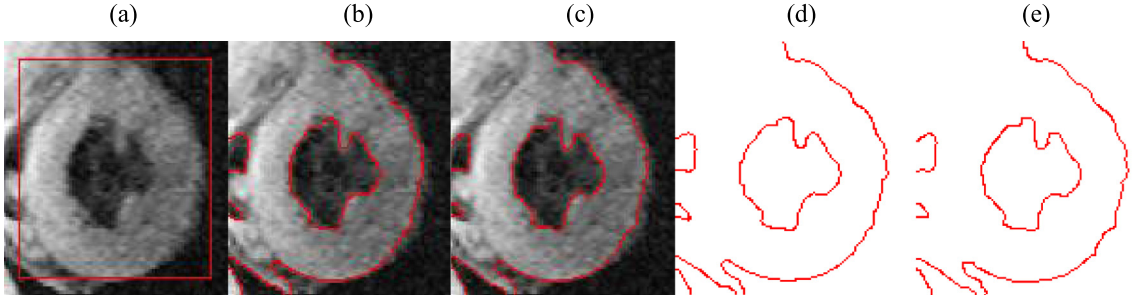


Fig. 5. Segmented results of an ultrasound image. (a) the original image with initial contour; (b) manual setting weighting; (c) adaptive weighting; (d) and (e) corresponding contour images of the segmented results ($\alpha = 0.6$, $\sigma_1 = 5$, $\mu = 0.1 \times 255 \times 255$).

where η is a given threshold. When the change of the area inside curve becomes smaller than a prescribed threshold η , the iteration will be stopped automatically. Thus, we can obtain a satisfactory segmented result with a sufficiently smaller threshold.

In addition to the stop criterion, in order to regularize the level set function efficiently and robustly, the Gaussian filtering strategy of Zhang et al. [27] is employed to ensure a smooth level set function in the evolution process. The standard deviation σ_2 of the Gaussian filtering can be used to control the regularization strength.

The procedures of the presented model can be summarized as follows:

- (1) Initialize the level set function $\varphi^0 (n=0)$ to be a binary function as

$$\phi^0 = \begin{cases} -1 & \text{if } x \in \Omega_0 - \partial\Omega_0 \\ 0 & \text{if } x \in \partial\Omega_0 \\ 1 & \text{if } x \in \Omega - \Omega_0 \end{cases}$$

Ω_0 is a subset in the image domain Ω and $\partial\Omega_0$ denotes the boundary of Ω_0 .

- (1) Calculate the difference image u_{ij} and the adaptive weighting w_{ij} by Eqs. (20) and (25).
- (2) Calculate $c_1(\varphi^n)$, $c_2(\varphi^n)$, $m_{1,i,j}(\varphi^n)$, $m_{2,i,j}(\varphi^n)$ by Eqs. (3) and (22).
- (3) Obtain the level set function φ^{n+1} by Eq. (28).
- (4) Smooth the level set function φ^{n+1} with Gaussian filter.
- (5) Check whether the evolution is stationary by Eq. (29). If not, $n = n + 1$ and return to step (3).

4. Experimental results

In this section, we report experimental results from segmentation of various synthetic and real images. We also compare results of the proposed model with the LCV model [8], the LBF model [15], the LIF model [31], the SBGFRLS model [27] and LSACM model [32]. All algorithms were implemented in Matlab R2010a on a computer with Intel Core i3-2310 M 2.10 GHz CPU, 2 G RAM, and Windows 32 operating system. In each experiment, we chose the time-step $\Delta t = 0.1$, the grid spacing $h = 1$, $\varepsilon = 1$, the threshold value $\eta = 1$, the maximum iteration $M = 100$, the local window size in the adaptive weighting $N = 3$, the standard deviation of the Gaussian kernel in regularizing the level set function $\sigma_2 = 0.6$. The standard deviation σ_1 of the Gaussian kernel in the local term, the order number α and the length term parameter μ are set to different values according to different image features.

The dice similarity coefficient (DSC) metric [33] is employed to evaluate quantitatively the segmented results of synthetic images. For a given baseline foreground region (e.g., true object) S_1 and the foreground region S_2 found by the models, the DSC metric is defined as:

$$DSC = \frac{2N(S_1 \cap S_2)}{N(S_1) + N(S_2)} \quad (30)$$

where $N(\cdot)$ indicates the number of pixels in the enclosed region. The closer the DSC value is to 1, the better the segmentation is. It means that a perfect segmentation result will be obtained when $DSC = 1$.

Fig. 5 demonstrates the validity of the adaptive weighting parameters. Fig. 5(a) is the original ultrasound image with initial contour [27], Fig. 5(b) is the segmented result with parameter $w = 0.5$, the manual setting weighting is obtained through many experiments. Fig. 5(c) is the segmented result with adaptive weighting parameters. We can see that Fig. 5(d) and (e) are almost the same. In addition, DSC values of Fig. 5(b) and (c) are 0.9921, and the results are very satisfactory. Hence, the proposed adaptive weighting parameter is right and effective, and can be automatically adjusted between the global term and the local term.

Fig. 6 illustrates the variation of gray values in the middle row of the original heart CT images [34] and three noisy images. We can see that the image pixel intensity becomes inhomogeneous due to the influence of noise. The corresponding

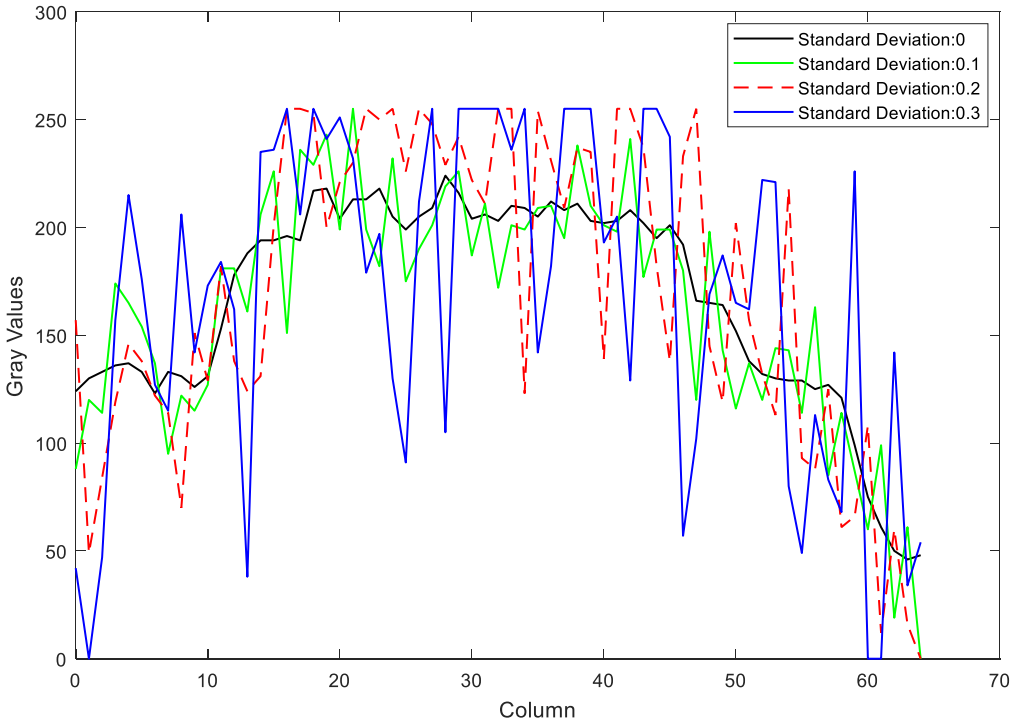


Fig. 6. The gray values of the middle row in the heart CT images with Gaussian noise of standard deviation 0.1, 0.2, 0.3 separately.

Table 1
The DSC values of the segmented results with different models.

DSC values	LIF	SBGFLS	LSACM	LCV	Proposed
Standard Deviation: 0.1	0.6516	0.9334	0.9541	0.9593	0.9686
Standard Deviation: 0.2	0.6864	0.8524	0.9226	0.9274	0.9559
Standard Deviation: 0.3	0.6374	0.8615	0.8767	0.9159	0.9303

segmented results and DSC values are shown in Fig. 7, and Table 1. The proposed model can obtain better segmented results than the traditional models, not only in the visual assessment, but also in quantitative DSC values.

Fig. 8 demonstrates the sensitivity of the proposed method for different initial contours. The first row shows the original medical images [35] with different initial contours, and the second row are corresponding segmented results. We can observe that the initial contours contain different shapes, sizes, and positions. However, our method still obtained satisfactory segmented results, showing robustness to the initial contour.

Fig. 9 shows the segmentation results for a real microscope cell image [27]. In the first row, the initial contour of the image contains two cells (see Fig. 9(a)), Fig. 9(b)–(f) are the corresponding segmented results with LBF model, SBGFLS model, LCV model, LSACM model, and the proposed model, separately. In the second row, the initial contour of the image includes only one cell (see Fig. 9(g)), Fig. 9(h)–(l) are the corresponding segmental results with the above five methods. For LBF model, the standard variation of the Gaussian kernel and the length parameter of the curve are respectively set as 7 and $0.02 \times 255 \times 255$ in Fig. 9(b), 20 and $0.02 \times 255 \times 255$ in Fig. 9(h). For the SBGFLS model, according to the experimental instruction in lecture [24], we set time-step $\Delta t = 1$, $\varepsilon = 1.5$, and the constant velocity term $\alpha = 20$ in Fig. 9(c) and (i). For LCV model, the size of the average filter and the length parameter of the curve are also respectively set as 3 and $0.02 \times 255 \times 255$ in Fig. 9(d) and (j), and the local weighting is equal to the global weighting. For the LSACM model, timestep is set as 1, the standard variations of the Gaussian kernel are set as 5 and 4 in Fig. 9(e), Fig. 9(k), separately. For the proposed model, the standard deviation σ_1 of the Gaussian kernel in the local term, the order number α and the length term parameter μ are set as 10, 0.7, $0.02 \times 255 \times 255$ in Fig. 9(f), and 15, 0.9, $0.02 \times 255 \times 255$ in Fig. 9(l). As shown in Fig. 9 and Table 2, the proposed model achieves satisfying segmented results for images with different initial contours.

Fig. 10 shows the segmentation results of different models on a hand phantom with the two middle fingers stuck together [31]. The first row shows the corresponding segmented results with the LBF model, the LCV model and the proposed model separately. For the LBF model, the standard variation of the Gaussian kernel and the length parameter of the curve are respectively set as 5 and $0.01 \times 255 \times 255$. For the LCV model, the size of the average filter and the length parameter of the curve are also respectively set as 3 and $0.01 \times 255 \times 255$, and the local weighting is equal to the global weighting. The

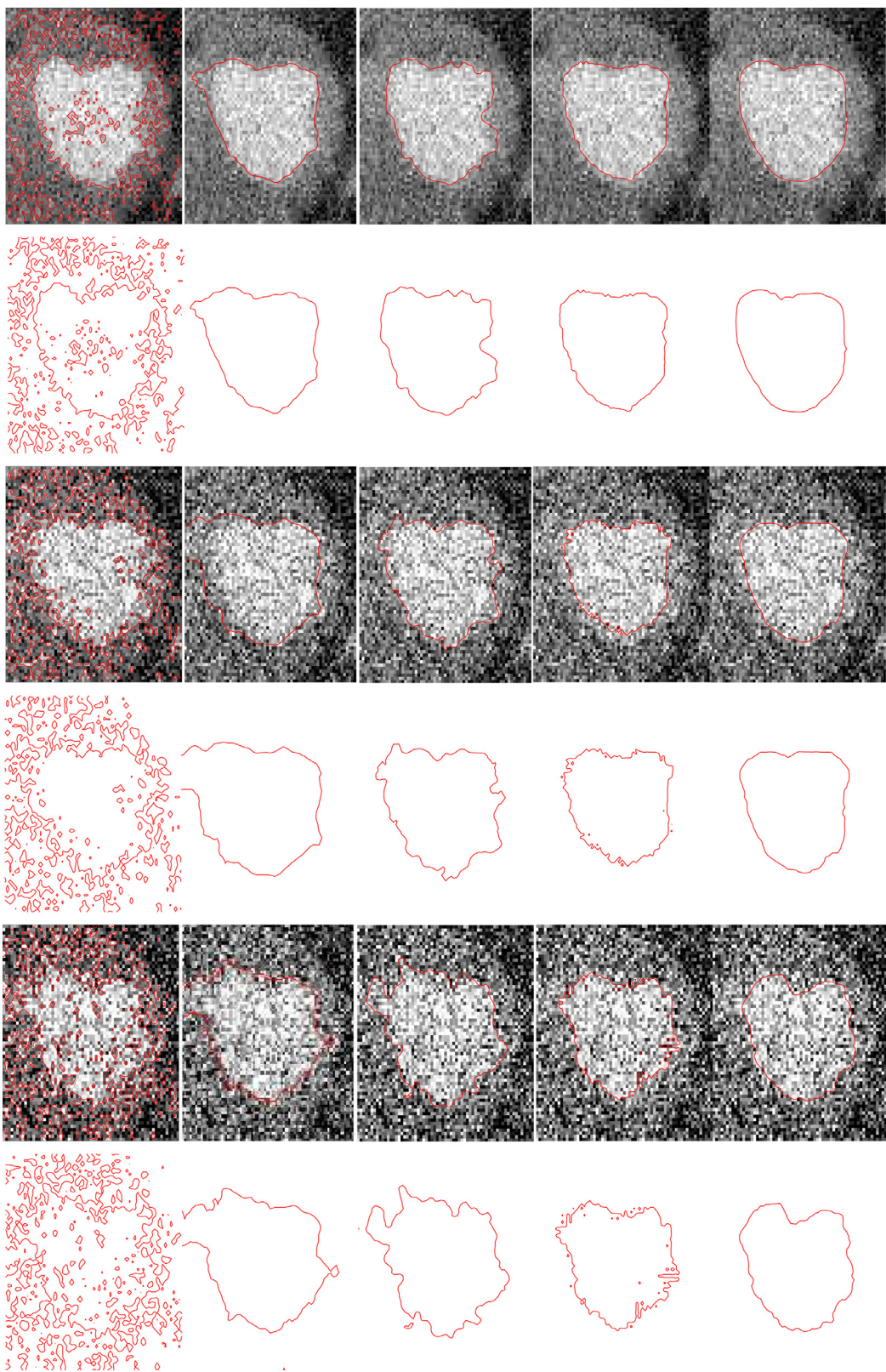


Fig. 7. Segmented results of a heart CT image with different Gaussian noise levels. The rows are the results of image with noise of standard deviation 0.1, 0.2, 0.3 separately (the even rows are the corresponding contours of the segmented results) and the 5 columns are the corresponding segmented results of LIF model, SBGFLRS model, LSACM model, LCV model and the proposed model.

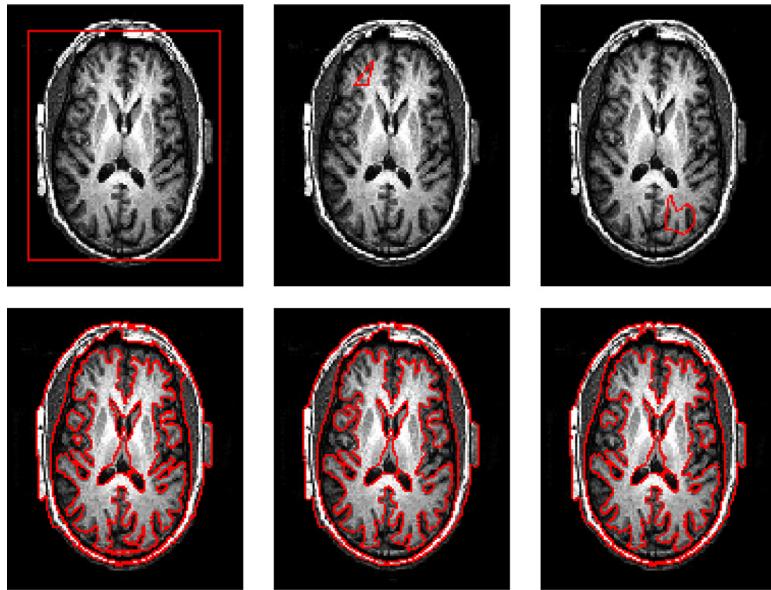


Fig. 8. Segmented results from a medical image with different initial contours. The first row shows the medical images with different initial contours; the second row shows the corresponding segmented results ($\alpha = 0.3$, $\sigma_1 = 3$, $\mu = 0.07 \times 255 \times 255$).

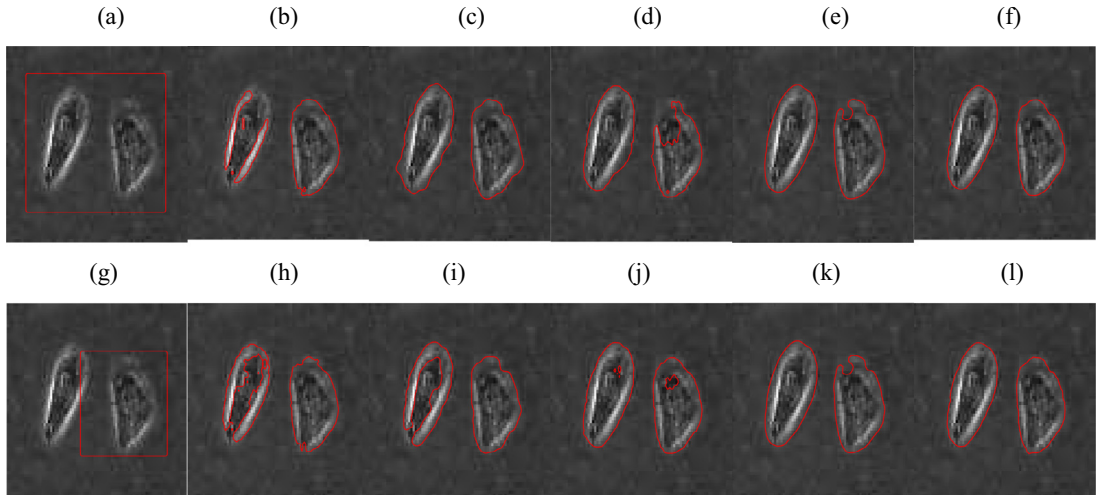


Fig. 9. Segmented results of a real microscope cell image with different initial contours. The first column: original image with different initial contours; The second to six columns: the corresponding segmented results of LBF model, SBGFLS model, LCV model, LSACM model and the proposed model, separately.

Table 2
The DSC values of the segmented results by different models with different initial contour.

DSC values	LBF	SBGFLS	LCV	LSACM	Proposed
Contour 1 (the first row in Fig. 5)	0.7486	0.8944	0.8459	0.8902	0.9272
Contour 2 (the second row in Fig. 5)	0.8196	0.8125	0.9139	0.8908	0.9266

third row presents the zoomed view of the narrow parts between two figures stuck together, it clearly demonstrates the good performance of our model in sub-pixel segmentation. Fig. 11 shows the change of the area within the evolution curve, when the evolution curve become stable, the areas error will gradually near to 0. As shown in Figs. 10 and 11, the proposed method can accurately achieve sub-pixel segmentation and make the two middle fingers apart with faster convergence than the traditional models.

Fig. 12 shows the segmented results of an inhomogeneous MRI image [32] by using different models. Fig. 12(a) is the original image with initial contour and its boundary is not obvious. Fig. 12(b)–(d) are the corresponding segmented results with the LBF model, the LCV model and the proposed model. For the LBF model, the standard variation of the Gaussian

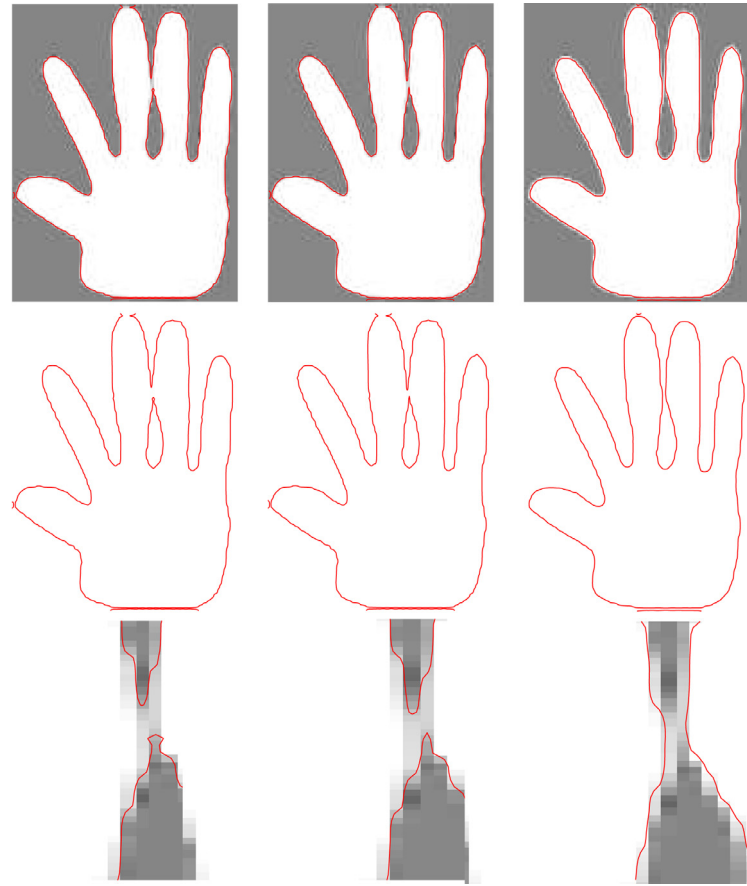


Fig. 10. Segmented results in a hand phantom image with different models. The first row: the corresponding segmented results with the LCV, the LBF and the proposed method; the second row: the corresponding contour images of the segmented results; the third row: the zoomed view of the narrow parts in the first row, respectively.

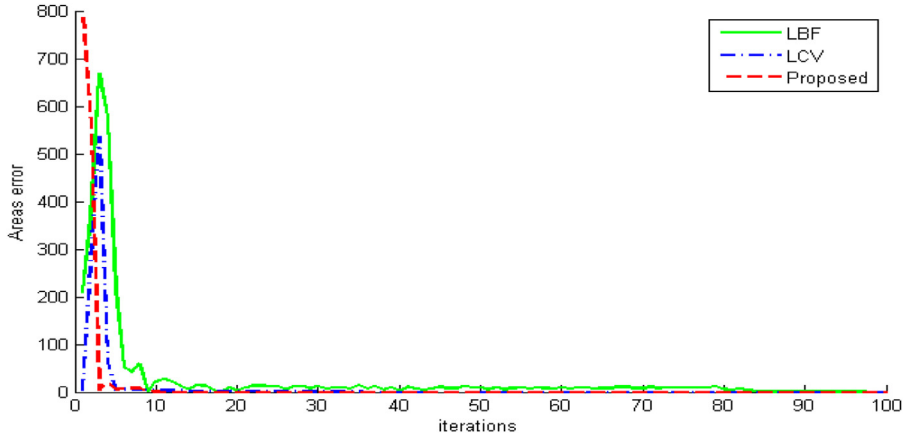


Fig. 11. The plotting comparison of different methods ($\alpha = 0.9$, $\sigma_1 = 5$, $\mu = 0.01 \times 255 \times 255$).

kernel and the length parameter of curve are set as 10 and $0.02 \times 255 \times 255$ separately. For the LCV model, the size of the average filter and the length parameter of the curve are also respectively set as 3 and $0.01 \times 255 \times 255$. From the segmented results, the proposed model can obtain more accurate results than the LBF and the LCV model.

Fig. 13 shows the segmented results from two galaxy images [27] by the proposed model. The first to third columns show the segmented results with LCV model, SBGFLS model, and the proposed model, respectively. We observe that better results can be obtained with the proposed model.

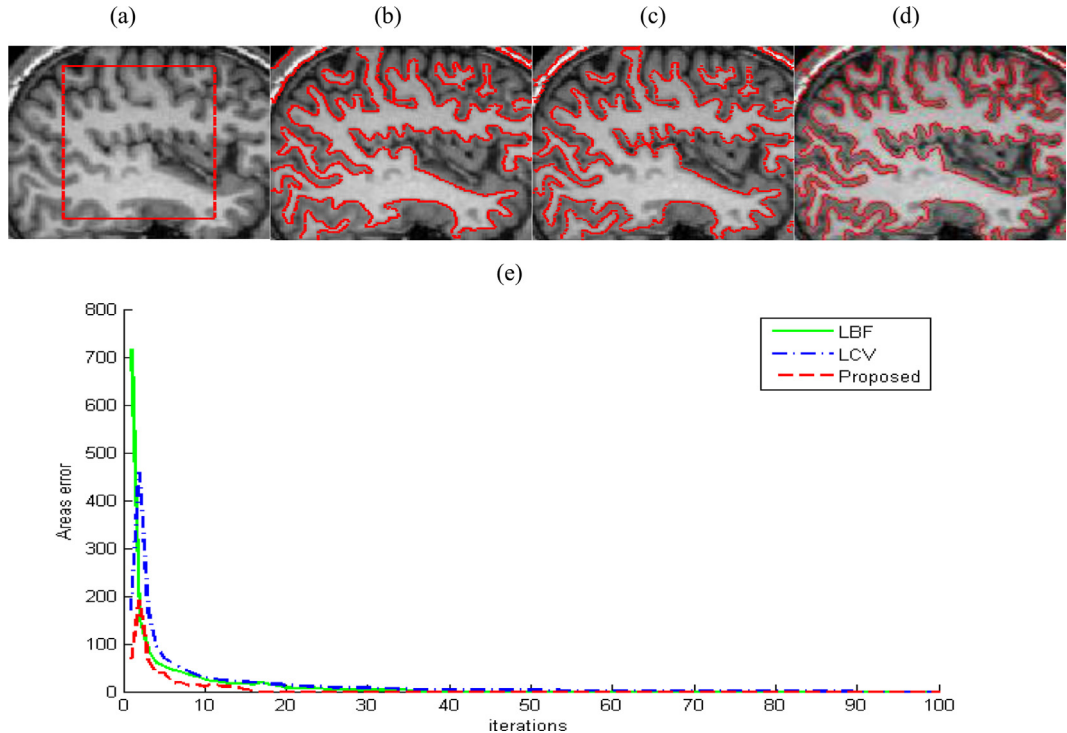


Fig. 12. Segmented results from the MRI image with different models. (a) the original image with initial contour; (b) and (d) the corresponding segmented results with the LBF, LCV and the proposed method; (e) the plotting comparison of different methods ($\alpha = 0.3$, $\sigma_1 = 3$, $\mu = 0.02 \times 255 \times 255$).

Table 3
The comparison of iterations and computational time for different method.

Image (size)	LBF model		LCV model		Our model	
	Iteration number	CPU time(s)	Iteration number	CPU time(s)	Iteration number	CPU time(s)
Fig. 11(130 × 108)	97	1.7004	35	2.2776	10	0.7332
Fig. 12(91 × 122)	36	2.0748	89	7.1448	16	1.3104

In order to evaluate the computational speed fairly, we also adopted the automatic stopping criterion (see Eq. (29)) for the LCV and the LBF models, and also set the threshold as 1. As shown in Table 3, Figs. 11, and 12(e), the needed numbers of iterations for our method were respectively 10 and 16. Our method was faster to achieve convergence than LCV and LBF, indicating that our method is more advantageous than LCV model in computational time.

5. Conclusion

Image segmentation algorithm has been studied continuously for several decades, thousands of various types of segmentation algorithms have been proposed with the help of various theories. However, due to there is still no universal segmentation theory, the proposed segmentation algorithms are mostly aimed at specific problems, and universal segmentation algorithm that is suitable for all images does not yet exist. In this paper, we proposed a novel adaptive weighting active contour model which integrates the fractional order differentiation, the fractional order gradient magnitude, and the difference image into a level set framework of segmenting inhomogeneity images. An adaptive parameter setting is investigated, which can adjust the weighting of the global and local terms automatically in the level set framework. The proposed model was robust to noisy and showed satisfactory performance for inhomogeneous image segmentation. For algorithm implementation, we adopt a new stopping criterion based on the area change inside the evolving curve. Experiment results on both synthetic and real images demonstrated that our method can segment images with inhomogeneous intensity distributions efficiently. However, experiments find that proposed model does not do a superior job on the uneven illuminated image segmentation, which is our research direction in next step. Prior information, which is given directly or training for example images, may be helpful for uneven illuminated image segmentation. In addition, the selection of parameters is still a challenging problem in the field of engineering applications. In this paper, the order of the fractional order differentiation α and other parameters are obtained manually through experiments or experience. α usually is set to 0.3, 0.6 or 0.9 for better segmentation results.

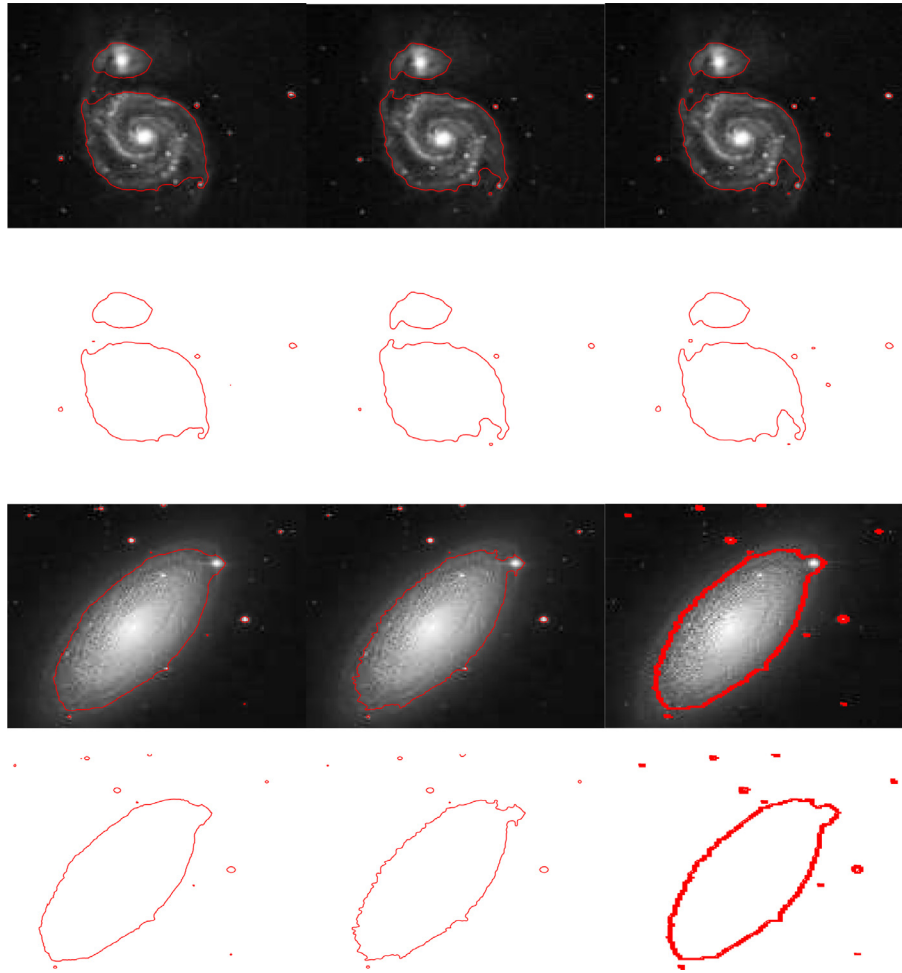


Fig. 13. Segmented results from two galaxy images. The first column shows the segmented results with LCV model; the second column shows the segmented results with SBGFLS model; the third column shows the segmented results with the proposed model ($\alpha = 0.3$, $\sigma_1 = 5$, $\mu = 0.015 \cdot 255 \cdot 255$); the second and fourth rows show the corresponding contour images of the segmented results.

Acknowledgment

This paper is partially supported by the Natural Science Foundation of Guangdong Province (2018A030313364), the Science and Technology Planning Project of Shenzhen City (JCYJ20140828163633997), the Natural Science Foundation of Shenzhen (JCYJ20170818091621856) and the China Scholarship Council Project (201508440370). Bo Chen would also like to thank Prof. Jianhua Ma from Southern Medical University and Prof. Xiangjun Kong from Qufu Normal University for their suggestions.

Appendix A. Derivation of the gradient descent flow

In this appendix, we deduce the corresponding gradient descent flow of the energy functional in Eq. (23) by using variational method [36,37] and gradient descent flow method. Eq. (23) can be expressed as following

$$\tilde{E}(\phi) = \int_{\Omega} \left\{ (1-w)[|I(X) - c_1|^2 H_\varepsilon(\phi) + |I(X) - c_2|^2 (1 - H_\varepsilon(\phi))] + w[|u(X) - m_1(X)|^2 H_\varepsilon(\phi) + |u(X) - m_1(X)|^2 (1 - H_\varepsilon(\phi))] + \mu \delta_\varepsilon(\phi) |\nabla \phi| \right\} dX \quad (31)$$

Let $F(x, y, \phi, \phi_x, \phi_y)$ denote the integrand of the above integral, then

$$\tilde{E}(\phi) = \int_{\Omega} F(x, y, \phi, \phi_x, \phi_y) dx dy \quad (32)$$

We add the perturbation $v(x, y)$ to the level set function ϕ , such that $\tilde{\phi}(x, y) = \phi(x, y) + v(x, y)$. When v, v_x, v_y is small enough, we can obtain the following formulation by Taylor's development

$$F(x, y, \phi + v, \phi_x + v_x, \phi_y + v_y) = F(x, y, \phi, \phi_x, \phi_y) + \frac{\partial F}{\partial \phi} v + \frac{\partial F}{\partial \phi_x} v_x + \frac{\partial F}{\partial \phi_y} v_y + \dots$$

Then $E(\tilde{\phi}) = E(\phi) + \int_{\Omega} v \frac{\partial F}{\partial \phi} + v_x \frac{\partial F}{\partial \phi_x} + v_y \frac{\partial F}{\partial \phi_y} dx dy$, according to subsection integration, we have

$$\int_{\Omega} v_x \frac{\partial F}{\partial \phi_x} dx dy = - \int_{\Omega} v \frac{d}{dx} \left(\frac{\partial F}{\partial \phi_x} \right) dx dy, \quad \int_{\Omega} v_y \frac{\partial F}{\partial \phi_y} dx dy = - \int_{\Omega} v \frac{d}{dy} \left(\frac{\partial F}{\partial \phi_y} \right) dx dy,$$

then

$$E(\tilde{\phi}) = E(\phi) + \int_{\Omega} v \frac{\partial F}{\partial \phi} - v \frac{d}{dx} \left(\frac{\partial F}{\partial \phi_x} \right) - v \frac{d}{dy} \left(\frac{\partial F}{\partial \phi_y} \right) dx dy \quad (33)$$

When $\tilde{E}(\phi)$ reach to its extremum, the value of \tilde{E} is kept unchanged for any sufficiently small perturbation $v(x, y)$, thus we have

$$\frac{\partial F}{\partial \phi} - \frac{d}{dx} \left(\frac{\partial F}{\partial \phi_x} \right) - \frac{d}{dy} \left(\frac{\partial F}{\partial \phi_y} \right) = 0 \quad (34)$$

[Eq. \(34\)](#) is the associated Euler equation of [Eq. \(32\)](#). The solution of the Euler equation can be regard as the extremum of the energy functional in [\(32\)](#). Next, we deduce the solution of the Euler equation in [\(34\)](#) by utilizing the gradient descent flow method.

By introducing an artificial time t , the static nonlinear PDE problem is transformed into a dynamic PDE problem. Let the perturbation $v(x, y)$ is a variation generated by $\varphi(x, y, t)$ from time t to time $t + \Delta t$, then $v = \frac{\partial \phi}{\partial t} \Delta t$. [Eq. \(33\)](#) can be expressed as following

$$E(\tilde{\phi}, t + \Delta t) = E(\phi, t) + \Delta t \int_{\Omega} \frac{\partial \phi}{\partial t} \left[\frac{\partial F}{\partial \phi} - \frac{d}{dx} \left(\frac{\partial F}{\partial \phi_x} \right) - \frac{d}{dy} \left(\frac{\partial F}{\partial \phi_y} \right) \right] dx dy$$

If we let

$$\frac{\partial \phi}{\partial t} = - \left[\frac{\partial F}{\partial \phi} - \frac{d}{dx} \left(\frac{\partial F}{\partial \phi_x} \right) - \frac{d}{dy} \left(\frac{\partial F}{\partial \phi_y} \right) \right] = \frac{d}{dx} \left(\frac{\partial F}{\partial \phi_x} \right) + \frac{d}{dy} \left(\frac{\partial F}{\partial \phi_y} \right) - \frac{\partial F}{\partial \phi}, \quad (35)$$

then have

$$\Delta E = E(\tilde{\phi}, t + \Delta t) - E(\phi, t) = - \Delta t \int_{\Omega} \left[\frac{\partial F}{\partial \phi} - \frac{d}{dx} \left(\frac{\partial F}{\partial \phi_x} \right) - \frac{d}{dy} \left(\frac{\partial F}{\partial \phi_y} \right) \right]^2 dx dy \leq 0 \quad (36)$$

[Eq. \(36\)](#) denote that the value of $E(\tilde{\phi}, t)$ is decrease steadily with the change of time. [Eq. \(35\)](#) is called the associated gradient descent flow of the energy functional $E(\tilde{\phi})$ in [Eq. \(32\)](#).

For a given initial function, the stationary solution of the gradient descent flow in [\(35\)](#) can be obtained by calculating the iterative formulation of [Eq. \(35\)](#). The stationary solution of the gradient descent flow in [\(35\)](#) is also the solution of the Euler equation in [\(34\)](#).

According to [Eqs. \(34\)](#) and [\(35\)](#), we can obtain the related Euler equation and gradient descent flow of the proposed energy functional:

$$\frac{\partial F}{\partial \phi} = (1 - w) [|I(X) - c_1|^2 - |I(X) - c_2|^2] \delta_{\varepsilon}(\phi) + w [|u(X) - m_1(X)|^2 - |u(X) - m_1(X)|^2] \delta_{\varepsilon}(\phi),$$

$$\frac{\partial F}{\partial \phi_x} = \mu \delta_{\varepsilon}(\phi) \frac{\phi_x}{\sqrt{\phi_x^2 + \phi_y^2}} = \mu \delta_{\varepsilon}(\phi) \frac{\phi_x}{|\nabla \phi|}, \quad \frac{\partial F}{\partial \phi_y} = \mu \delta_{\varepsilon}(\phi) \frac{\phi_y}{\sqrt{\phi_x^2 + \phi_y^2}} = \mu \delta_{\varepsilon}(\phi) \frac{\phi_y}{|\nabla \phi|},$$

$$\frac{d}{dx} \left(\frac{\partial F}{\partial \phi_x} \right) = \mu \delta_{\varepsilon}(\phi) \frac{d}{dx} \left(\frac{\phi_x}{|\nabla \phi|} \right), \quad \frac{d}{dy} \left(\frac{\partial F}{\partial \phi_y} \right) = \mu \delta_{\varepsilon}(\phi) \frac{d}{dy} \left(\frac{\phi_y}{|\nabla \phi|} \right),$$

$$\begin{aligned} \frac{\partial \phi}{\partial t} &= - \frac{\partial F}{\partial \phi} + \frac{d}{dx} \left(\frac{\partial F}{\partial \phi_x} \right) + \frac{d}{dy} \left(\frac{\partial F}{\partial \phi_y} \right) \\ &= (1 - w) [-|I(X) - c_1|^2 + |I(X) - c_2|^2] \delta_{\varepsilon}(\phi) + w [-|u(X) - m_1(X)|^2 + |u(X) - m_1(X)|^2] \delta_{\varepsilon}(\phi) \\ &\quad + \mu \delta_{\varepsilon}(\phi) \left[\frac{d}{dx} \left(\frac{\phi_x}{|\nabla \phi|} \right) + \frac{d}{dy} \left(\frac{\phi_y}{|\nabla \phi|} \right) \right] \\ &= \delta_{\varepsilon}(\phi) \left\{ (1 - w) [-|I(X) - c_1|^2 + |I(X) - c_2|^2] + w [-|u(X) - m_1(X)|^2 + |u(X) - m_1(X)|^2] + \mu \operatorname{div} \left(\frac{\nabla \phi}{|\nabla \phi|} \right) \right\} \end{aligned}$$

References

- [1] L Li, F Meng, Z Zheng, Some new oscillation results for linear Hamiltonian systems, *Appl. Math. Comput.* 208 (1) (2009) 219–224.
- [2] L Liu, Y Bai, New oscillation criteria for second-order nonlinear neutral delay differential equations, *J. Comput. Appl. Math.* 231 (2) (2009) 657–663.
- [3] F Xu, L Liu, Y Wu, Multiple positive solutions of four-point nonlinear boundary value problems for higher-order p-Laplacian operator with all derivatives, *Nonlinear Anal.: Theory Method Appl.* 71 (9) (2009) 4309–4319.
- [4] V Caselles, R Kimmel, G Sapiro, Geodesic active contours, *Int. J. Comput. Vis.* 22 (1) (1997) 61–79.
- [5] N Paragios, R Deriche, Geodesic active contours and level sets for the detection and tracking of moving objects, *IEEE Trans. Pattern Anal. Mach. Intell.* 22 (3) (2000) 266–280.
- [6] T Chan, L Vese, Active contours without edges, *IEEE Trans. Image Process.* 10 (2) (2001) 266–277.
- [7] G Zhu, S Zhang, Q Zeng, et al., Boundary-based image segmentation using binary level set method, *Opt. Eng.* 46 (5) (2007) 050501–050501-3.
- [8] X Wang, D Huang, H Xu, An efficient local Chan–Vese model for image segmentation, *Pattern Recogn.* 43 (3) (2010) 603–618.
- [9] B Chen, Q Zou, W Chen, et al., A novel adaptive partial differential equation model for image segmentation, *Appl. Anal.* 93 (11) (2014) 2440–2450.
- [10] B Chen, Q Zou, Y Li, A new image segmentation model with local statistical characters based on variance minimization, *Appl. Math. Model.* 39 (12) (2015) 3227–3235.
- [11] M Kass, A Witkin, D Terzopoulos, Snakes: active contour models, *Int. J. Comput. Vis.* 1 (4) (1988) 321–331.
- [12] D Mumford, J Shah, Optimal approximations by piecewise smooth functions and associated variational problems, *Commun. Pure Appl. Math.* 42 (5) (1989) 577–685.
- [13] L Vese, T Chan, A multiphase level set framework for image segmentation using the Mumford and Shah model, *Int. J. Comput. Vis.* 50 (3) (2002) 271–293.
- [14] A Tsai, JRA Yezzi, AS. Willsky, Curve evolution implementation of the Mumford–Shah functional for image segmentation, denoising, interpolation, and magnification, *IEEE Trans. Image Process.* 10 (8) (2001) 1169–1186.
- [15] C Li, C Kao, J Gore, et al., Implicit active contours driven by local binary fitting energy, in: *Proceedings of the 2007 IEEE Conference on Computer Vision and Pattern Recognition*, 2007, pp. 1–7.
- [16] S Liu, Y Peng, A local region-based Chan–Vese model for image segmentation, *Pattern Recogn.* 45 (7) (2012) 2769–2779.
- [17] Z Wang, X Huang, G Shi, Analysis of nonlinear dynamics and chaos in a fractional order financial system with time delay, *Comput. Math. Appl.* 62 (3) (2011) 1531–1539.
- [18] Z. Wang, A numerical method for delayed fractional-order differential equations, *J. Appl. Math.* 2013 (2013) Article ID 256071, 7 pages.
- [19] Z. Wang, X. Huang, J. Zhou, A numerical method for delayed fractional-order differential equations: based on G-L definition, *Appl. Math. Inf. Sci.* 7 (2) (2013) 525–529.
- [20] J. Bai, X.C. Feng, Fractional-order anisotropic diffusion for image denoising, *IEEE Trans. Image Process.* 16 (10) (2007) 2492–2502.
- [21] Z Jun, W Zhihui, A class of fractional-order multi-scale variational models and alternating projection algorithm for image denoising, *Appl. Math. Model.* 35 (5) (2011) 2516–2528.
- [22] E Cuesta, M Kirane, A Malik S, Image structure preserving denoising using generalized fractional time integrals, *Signal Process.* 92 (2) (2012) 553–563.
- [23] B Mathieu, P Melchior, A Oustaloup, et al., Fractional differentiation for edge detection, *Signal Process.* 83 (11) (2003) 2421–2432.
- [24] A Nakib, H Oulhadj, P Siarry, A thresholding method based on two-dimensional fractional differentiation, *Image Vis. Comput.* 27 (9) (2009) 1343–1357.
- [25] Z. Ren, Adaptive active contour model driven by fractional order fitting energy, *Signal Process.* 117 (2015) 138–150.
- [26] C Li, C Xu, C Gui, et al., Level set evolution without re-initialization: a new variational formulation, in: *Proceedings of the IEEE Conference on Computer Vision and Pattern Recognition*, 1, 2005, pp. 430–436.
- [27] K Zhang, L Zhang, H Song, et al., Active contours with selective local or global segmentation: a new formulation and level set method, *Image Vis. Comput.* 28 (4) (2010) 668–676.
- [28] H Lv, Z Wang, S Fu, et al., A robust active contour segmentation based on fractional-order differentiation and fuzzy energy, *IEEE Access* 5 (2017) 7753–7761.
- [29] L Wang, C Li, Q Sun, et al., Active contours driven by local and global intensity fitting energy with application to brain MR image segmentation, *Comput. Med. Imaging Graph.* 33 (7) (2009) 520–531.
- [30] Y Yu, C Zhang, Y Wei, et al., Active Contour Method Combining Local Fitting Energy and Global Fitting Energy Dynamically Medical Biometrics, Springer, Berlin Heidelberg, 2010, pp. 163–172.
- [31] K Zhang, H Song, L Zhang, Active contours driven by local image fitting energy, *Pattern Recogn.* 43 (4) (2010) 1199–1206.
- [32] K Zhang, L Zhang, D Zhang, A level set approach to image segmentation with intensity inhomogeneity, *IEEE Trans. Cybern.* 46 (2) (2016) 546–557.
- [33] D Shattuck, S Sandor-Leahy, K Schaper, D Rottenberg, R Leahy, Magnetic resonance image tissue classification using a partial volume model, *Neuroimage* 13 (2001) 856–876.
- [34] Dietenbeck T, Alessandrini M, Friboulet D, Bernard O. CREASED: a free software for the evaluation of image segmentation algorithms based on level-set, in: *Proceedings of the 2010 Seventeenth IEEE International Conference on Image Processing (ICIP)*, Hong Kong, 26–29 September 2010, 665–668.
- [35] T Goldstein, X Bresson, S Osher, Geometric applications of the split bregman method: segmentation and surface reconstruction, *J. Sci. Comput.* 45 (1–3) (2010) 272–293.
- [36] J Liu, Z Zhao, An application of variational methods to second-order impulsive differential equation with derivative dependence, *Electron. J. Diff. Eq.* 2014 (62) (2014) 1–13.
- [37] J Liu, Z Zhao, Variational approach to second-order damped Hamiltonian systems with impulsive effects, *J. Nonlinear Sci. Appl.* 9 (2016) 3459–3472.